NANO · MICRO small
www.small-journal.com

MOF-Enabled Ion-Regulating Gel Electrolyte for Long-Cycling Lithium Metal Batteries Under High Voltage

Xuewei Fu, Matthew J. Hurlock, Chenfeng Ding, Xiaoyu Li, Qiang Zhang, and Wei-Hong Zhong**

High-voltage lithium metal batteries (LMBs) are a promising high-energy-density energy storage system. However, their practical implementations are impeded by short lifespan due to uncontrolled lithium dendrite growth, narrow electrochemical stability window, and safety concerns of liquid electrolytes. Here, a porous composite aerogel is reported as the gel electrolyte (GE) matrix, made of metal–organic framework (MOF)@bacterial cellulose (BC), to enable long-life LMBs under high voltage. The effectiveness of suppressing dendrite growth is achieved by regulating ion deposition and facilitating ion conduction. Specifically, two hierarchical mesoporous Zr-based MOFs with different organic linkers, that is, UiO-66 and NH_2-UiO-66, are embedded into BC aerogel skeletons. The results indicate that NH_2-UiO-66 with anionphilic linkers is more effective in increasing the Li^+ transference number; the intermolecular interactions between BC and NH_2-UiO-66 markedly increase the electrochemical stability. The resulting GE shows high ionic conductivity (≈1 mS cm^{-1}), high Li^+ transference number (0.82), wide electrochemical stability window (4.9 V), and excellent thermal stability. Incorporating this GE in a symmetrical Li cell successfully prolongs the cycle life to 1200 h. Paired with the Ni-rich $LiNiCoAlO_2$ (Ni: Co: Al = 8.15:1.5:0.35, NCA) cathode, the NH_2-UiO-66@BC GE significantly improves the capacity, rate performance, and cycle stability, manifesting its feasibility to operate under high voltage.

1. Introduction

The pursuit for higher-energy rechargeable batteries is being intensified as the current lithium-ion batteries (LIBs) are approaching their energy limit.[1,2] Lithium (Li) metal anode possesses ultrahigh theoretical capacity (3860 mAh g^{-1}), low bulk density (0.53 g cm^{-3}), and the lowest negative potential (−3.04 V vs the standard hydrogen electrode).[3] These intriguing advantages make Li metal a promising candidate to be paired with various high-capacity cathodes to generate greater energy than LIBs.[4–6] Unfortunately, unveiling the Li anode technology, in reality, is faced with several persistent challenges. The most significant hurdles are the prevalent safety concern and short lifespan caused by the electro–chemo–mechanical instability of Li metal that drives the uncontrollable growth of Li dendrites in repeated cyclic processes.[7] The self-amplified Li dendrites may pierce the separator and cause thermal runaway, short-circuiting, or even explosion.[8,9] Meanwhile, the solid electrolyte interphase (SEI) layer can be broken by Li dendrites, causing continuous consumption of electrolytes/Li sources and eventually, inferior cycle performance.[10]

Suppressing dendrite growth is a critical step before making the Li anode viable in the energy storage market. Extensive efforts have been made toward nanostructure design of Li anodes/current collectors,[11–13] or applying artificial SEI layers,[14,15] separator coatings,[16–18] solid/gel electrolytes,[19–21] electrolyte additives,[22,23] and so on. Among these modifications, solid electrolyte-enabled Li metal batteries (LMBs) are recognized as the ultimate choice because they eliminate the safety hazards resulting from leakage or explosion of organic liquid electrolytes;[24] the high mechanical modulus of solid electrolytes is also expected to alleviate the dendrite proliferation.[25] However, solid electrolytes are plagued by lower ionic conductivity and significantly greater interfacial resistance than liquid electrolytes.[26] Gel electrolytes (GEs) integrating the merits of relatively high ionic conductivity and good interfacial properties are regarded as a competent alternative to conquer the obstacles, and it is anticipated to soon broaden their applications practically.[27,28] For decades, a wide variety of GEs based on poly(vinylidene fluoride-co-hexafluoropropylene),[29,30] polyurethane,[31,32] polyacrylonitrile,[33,34] poly(ethylene oxide),[35,36] and more have been investigated to impart improved ionic conductivity at the order of magnitude close to liquid electrolytes (10^{-3} S cm^{-1}). However, GEs are less effective to suppress Li dendrites because of their insufficient modulus at the mega-Pascal

X. Fu, C. Ding, W.-H. Zhong
School of Mechanical and Materials Engineering
Washington State University
Pullman, WA 99164, USA
E-mail: katie_zhong@wsu.edu
M. J. Hurlock, Q. Zhang
Department of Chemistry
Washington State University
Pullman, WA 99164, USA
E-mail: q.zhang@wsu.edu
X. Li, Q. Zhang, W.-H. Zhong
Materials Science and Engineering Program
Washington State University
Pullman, WA 99164, USA

The ORCID identification number(s) for the author(s) of this article can be found under https://doi.org/10.1002/smll.202106225.

DOI: 10.1002/smll.202106225

level in comparison to solid electrolytes; it is suggested that a shear modulus twice of that of Li metal (≈3.4 GPa)[37] is a prerequisite, which is formidable to achieve.

Besides increasing the mechanical modulus, restricting the anion motion or increasing the Li^+ transference number can delay the onset of dendrite growth. This is dictated by the Sand's time model,[38] indicating that the depletion of anions near the Li anode surface causes an uneven electric field and initiates the nucleation of dendrites. Following this direction, several strategies have been exerted, such as adding anion-traps on polymer chains[39] or nanofillers (e.g., LATP,[40] SiO_2,[41] etc.) in polymer matrices. Recently, metal–organic frameworks (MOFs) have emerged as attractive, functional nanofillers owing to the high population of micro-/meso-pores and tunable organic ligands to impart the capability to store more liquid electrolytes and regulate the ion-transfer process.[42] The inertness of MOFs also benefits the interfacial stability of GEs.[43] To name a few, HKUST-1,[42] Mg-MOF-74,[44] UiO-66,[45] and ZIF-8[46] have been used as nanofillers to improve the ionic conductivity and Li^+ transference number. Despite the satisfactory ionic conductivity >1 mS cm^{-1}, these MOF-filled GEs exhibit moderate Li^+ transference numbers (≈0.6), meaning that more efforts are necessary to further improve the Li anode stability and then extend the battery lifespan.

Cellulose is one of the promising GE matrices owing to its rich hydroxyl groups that can generate strong binding with Li^+/electrolyte solvents and prevent the anion motion,[47,48] yielding great potential in increasing both ionic conductivity and Li^+ transference number. Additionally, cellulose exhibits good mechanical strength and thermal stability,[49,50] making it appropriate for battery applications under various operation conditions. To date, a variety of GEs from cellulose,[51–53] lignocellulose,[47,54,55] and methylcellulose[56,57] have been reported. The Li^+ transference numbers of the cellulose-derived GEs were proved remarkable, as high as 0.82.[52] Nonetheless, like polyethylene oxide (PEO), the ether oxygens from cellulose possibly generate side reactions with electrolyte solvents and Li salts under high voltage.[50,58,59] This drawback determines that cellulose-derived GEs can only be coupled with low-voltage cathodes such as $LiFePO_4$, leading to a limited energy density. However, high-voltage cathodes (e.g., Ni-rich/Li-rich cathodes) are the most promising to be widely implemented in practice today.[60,61]Therefore, compatibility only with low-voltage cathodes is the critical hurdle for cellulose-derived GEs.

In this study, we report an ion-regulating and high voltage-compatible bacterial cellulose (BC)/MOF composite aerogel as the GE matrix to stabilize LMBs. Two mesoporous Zr-based MOFs with different organic linkers are investigated, both enhancing the electrochemical/mechanical properties of the GEs. It is found that the NH_2-UiO-66 nanofiller increases the Li^+ transference number more than that of the UiO-66 counterpart, owing to the rationally designed anionphilic organic linkers. The synergistic effect from high-wettability porous BC skeleton and NH_2-UiO-66 yields high ionic conductivity (≈1 mS cm^{-1}), high Li^+ transference number (0.82), and a wide electrochemical stability window (4.9 V) for the resulting GE. As a result, a long-lifetime Li|Li cell with a cycling life of ≈1200 h is achieved. Coupled with the Ni-rich $LiNiCoAlO_2$ (Ni: Co: Al = 8.15: 1.5: 0.35, NCA) cathode, the NH_2-UiO-66@BC composite GE remarkably improves the capacity, rate performance, and cycle stability, demonstrating its feasibility to operate under high voltage.

2. Results and Discussion

The NH_2-UiO-66@BC GE matrix is fabricated by compositing entangled BC nanofibrils and NH_2-UiO-66 nanoparticles into a hierarchically porous-structured aerogel via freeze-drying and compressive-shaping, as shown in **Figure 1**a. The abundance of polar hydroxyl groups and hierarchical pore structures of the BC skeleton leads to excellent wettability and sufficient uptake for the liquid electrolyte. This establishes considerable pathways and facilitates ion conduction in the charge/discharge process. The Lewis acid sites of NH_2-UiO-66 (Zr^{4+}) promote the dissociation of Li salts by attracting the PF_6^- anions[62]; the PF_6^--philic groups ($-NH_2$) in the linkers serve as extra anion-immobilization sites, whose hydrogen atom is prone to form hydrogen bonding with the fluorine atom of PF_6^-.[47,63] It is known that ions in the electrolyte tend to concentrate near the pores of the separator, leading to inhomogeneous ion deposition and dendrite formation (Figure 1a). On the contrary, with the NH_2-UiO-66@BC GE, the ion-conduction process is accelerated, and the ion deposition is homogenized to prevent the dendrite growth.

Two Zr-based MOFs with different organic linkers, UiO-66 with BDC (terephthalate) linker and NH_2-UiO-66 with NH_2-BDC (ammino-terephthalate) linker, are incorporated, respectively to the BC skeleton. These two MOFs are advantageous in thermal and chemical stabilities.[64] The X-ray diffraction (XRD) patterns in Figure S1, Supporting Information, show characteristic diffraction peaks of UiO-66 and NH_2-UiO-66, which are consistent with literature[65] and indicate the successful formation of the MOFs. As shown in Figure 1b,c, small NH_2-UiO-66 nanoparticles with a size of ≈10 nm aggregate to form monoliths that are a few hundred nanometers in size, generating numerous pores. UiO-66 shows similar morphological features as indicated by the transmission electron microscope (TEM) images in Figure S2, Supporting Information. The chemical groups of the two MOFs are probed by Fourier-transform infrared spectroscopy (FTIR), and the results are shown in Figure 1d. For UiO-66, theabsorption peaks at 1395 and 1583 cm^{-1} correspond to the coordinated C—O stretching, while the peak at 1502 cm^{-1} is due to C=C stretching from the benzene ring. All the peaks are characteristic of the BDC linker. In addition to them, more absorption peaks are observed for NH_2-UiO-66. The two peaks located at 1336 and 1254 cm^{-1} are both attributed to C—N stretching, and the peak at 1655 cm^{-1} can be assigned to N—H bending. The result verifies the presence of the $-NH_2$ group in NH_2-UiO-66, which is endowed by the NH_2-BDC linker. The pore structures of the MOFs are characterized by N_2 adsorption/desorption analysis. As shown in Figure S3, Supporting Information, the N_2 sorption isotherms exhibit Type IV isotherm and type II hysteresis loops according to the IUPAC classification, indicating the existence of micropores and mesopores; the large loops suggest broad pore size distributions. The Brunauer–Emmett–Teller (BET) surface areas of UiO-66 and NH_2-UiO-66 are 1158 and 724 m^2 g^{-1}, respectively. The pore size distribution

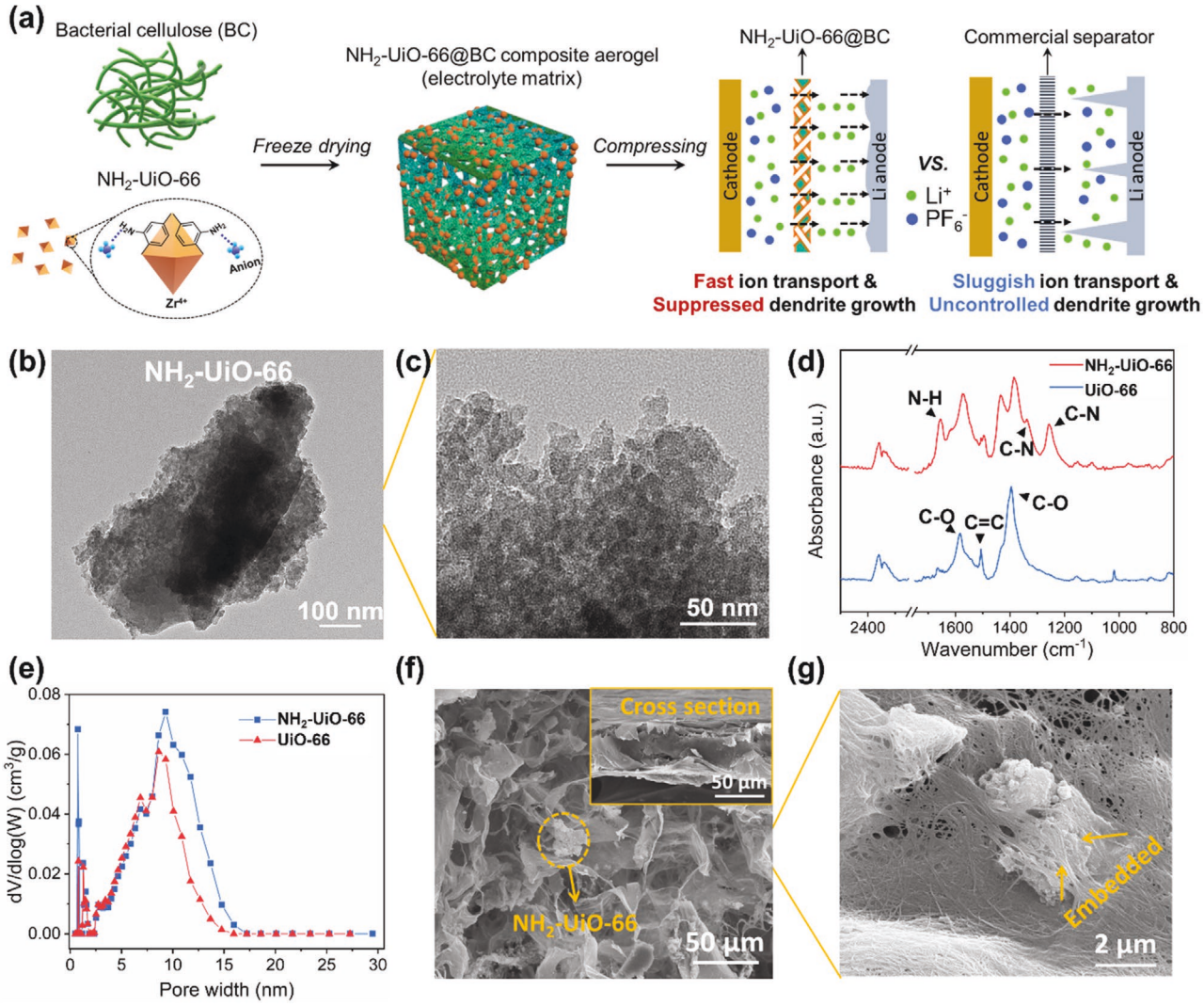

Figure 1. Fabrication and morphological properties of NH_2-UiO-66@BC composite aerogel as the GE matrix. a) Schematic illustration of the fabrication of NH_2-UiO-66@BC composite aerogel as the GE matrix and the contribution to the ion-transfer process in a battery. b,c) TEM images of NH_2-UiO-66 at different magnifications. d) FTIR spectra of NH_2-UiO-66 and UiO-66. e) DFT pore size distribution of NH_2-UiO-66 and UiO-66. f,g) SEM images of NH_2-UiO-66@BC at different magnifications.

is calculated by the density functional theory (DFT) model in Figure 1e. As shown, the most populated distributions of the mesopores lie at 9.3 and 8.6 nm for UiO-66 and NH_2-UiO-66, respectively. The massive amount of mesopores will facilitate the infiltration of the liquid electrolyte.

Figure S4, Supporting Information, shows the scanning electron microscope (SEM) images of the BC aerogel, which reveal the hierarchical porous architectures with pores of a broad range from micro-scale to nano-scale. The microstructure of MOF@BC composite aerogels is similar to the original BC aerogel, which also exhibits a hierarchically porous structure in Figure 1f (also see SEM images of UiO-66@BC aerogel in Figure S5, Supporting Information). The cross-sectional SEM image in Figure 1f shows that the thickness of the composite aerogel is about 60 μm after compression, which is appropriate for GE applications in batteries. When taking a closer look, we observed that the NH_2-UiO-66 nanoparticles are embedded into the BC nanofibril cell walls in Figure 1g, which is due to the strong entanglement effect between the MOF nanoparticles and BC nanofibrils. The loadings of the MOFs are kept constant at ≈20 wt%, as indicated by the thermogravimetric analysis (TGA) result in Figure S6, Supporting Information.

The hierarchically porous structure and rich polar groups of the composite aerogel effectively increase the adsorption and uptake of liquid electrolytes (see the FTIR spectrum of BC aerogel in Figure S7, Supporting Information, indicating the existence of —OH and C—O groups). As shown in **Figure 2**a, the electrolyte droplet on the nonpolar commercial separator (CS) undergoes a slow wetting process, resulting in a significant equilibrium contact angle of 56.2°. By contrast, the electrolyte droplet completely infiltrates the NH_2-UiO-66@BC composite aerogel intermediately after the droplet contacts the surface. Similar results are also obtained from BC and UiO-66@BC in Figure S8, Supporting Information. The electrolyte uptake of

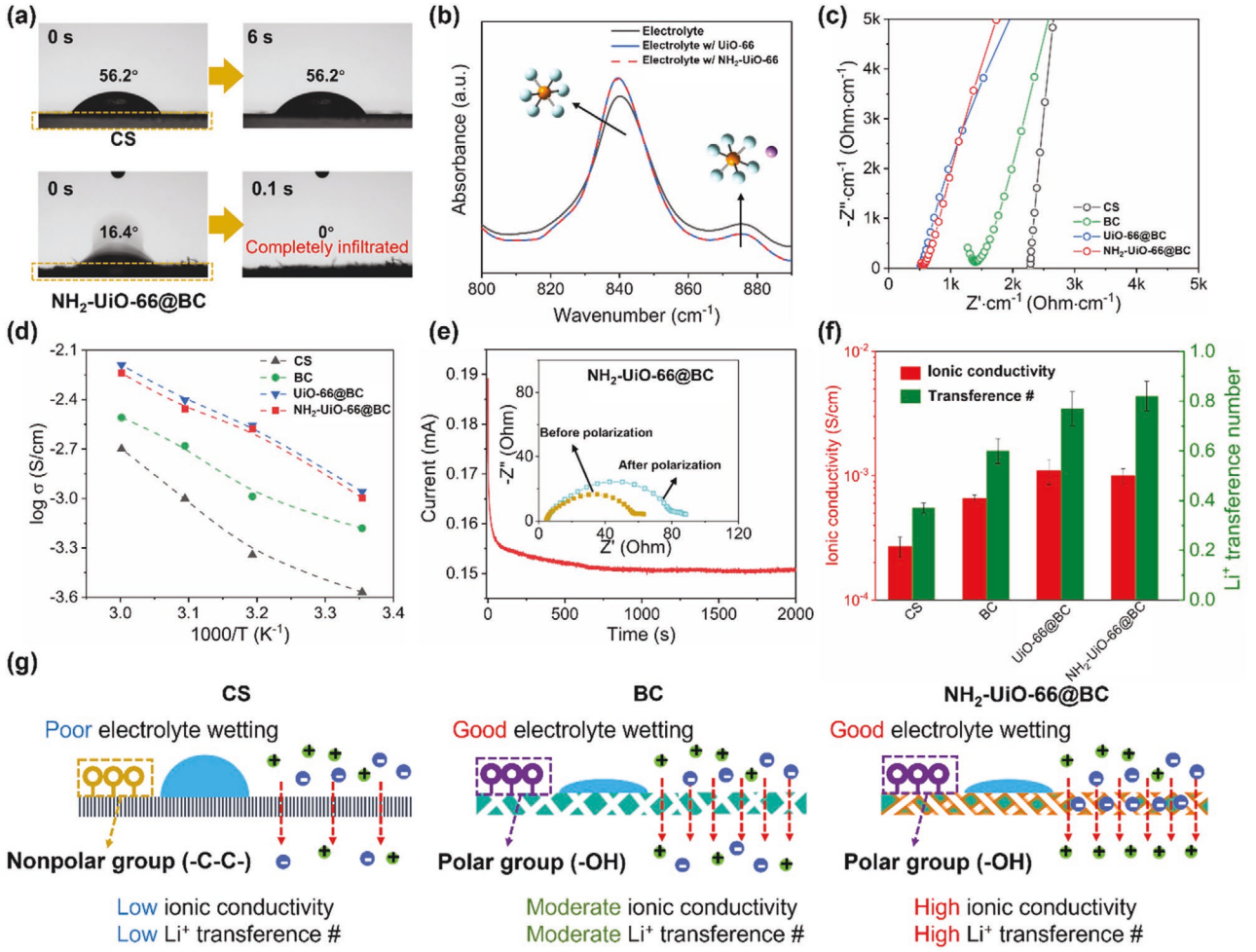

Figure 2. Wetting behavior and electrochemical properties of GEs. a) The contact angle of the liquid electrolyte on the nonpolar commercial separator (top), and the NH_2-UiO-66@BC composite aerogel (bottom). b) FTIR spectra of the liquid electrolyte with or without MOFs. c) Nyquist plots of various GEs compared to CS. The samples were sandwiched by two stainless plates of steel for the measurement. d) Ionic conductivity as a function of temperature. e) Chronoamperometric curves and Nyquist plots before and after the polarization. f) Summary of ionic conductivity and Li^+ transference number for various GEs compared to CS. g) Schematic illustration of the wetting behavior and the ion diffusion process across CS (commercial separator), BC, and NH_2-UiO-66@BC.

various aerogels compared with CS is presented in Table S1, Supporting Information. Benefiting from the 3D porous structure of the BC aerogel skeleton and the hydroxyl groups to render electrolyte affinity, the electrolyte uptake of BC aerogel reaches 429% ± 13%, much greater than that of CS (87 ± 2%). When the mesoporous MOFs are embedded into the BC aerogels, the electrolyte uptake is further increased: 690% ± 20% for UiO-66@BC and 634% ± 23% for NH_2-UiO-66@BC. This is because the numerous mesopores of MOFs adsorb more liquid electrolytes, which is beneficial to increase the ionic conductivity of the resulting GEs.

It is reported that the Lewis acid sites on MOFs help the dissociation of Li salts,[62] potentially increasing the ionic conductivity of the electrolyte. To probe the effect of MOFs on the ion dissociation, a certain amount of MOF nanoparticles are added in the liquid electrolytes composed of 1 M $LiPF_6$ dissolved in ethyl carbonate (EC)/ethyl methyl carbonate (EMC) (1/1 by volume). The FTIR spectra on the anion–cation coordination for the various electrolytes are presented in Figure 2b. Two P—F stretching peaks can be found in the spectra: the one at 840 cm^{-1} is attributed to solvent separated ion pair (SSIP) and contact ion pair (CIP), while the one at 879 cm^{-1} is attributed to the cation-coordinated PF_6^-.[66] As shown, there is a variation of peak intensities after MOFs are added to the electrolytes. Specifically, the intensity of the peak at 879 cm^{-1} is obviously decreased for both UiO-66 and NH_2-UiO-66 samples. The results suggest that the PF_6^- anions are better dissociated by the two MOFs because the Zr^{4+} Lewis acidic centers attract the anions to help their dissociation from Li^+ cations. Accordingly, the ionic conductivity of the MOF@BC composite GEs is greatly increased, as shown in Figure 2c. It can be seen that the bulk resistance increases following the order of UiO-66@BC, NH_2-UiO-66@BC, BC, and CS. To gain a deeper insight, the ionic conductivity at various temperatures is measured and presented in Figure 2d. All GEs and CS experience a significant increase of ionic conductivity with temperature. Throughout the temperature range, UiO-66@BC shows the highest ionic conductivity, followed by NH_2-UiO-66@BC, BC, and CS. At

25 °C, the ionic conductivity of UiO-66@BC and NH_2-UiO66@BC is 1.1 and 1.0 mS cm^{-1}, respectively, much greater than CS (0.27 mS cm^{-1}) and BC (0.66 mS cm^{-1}). At an elevated temperature of 40 °C, UiO-66@BC and NH_2-UiO-66@BC show remarkable ionic conductivity of 3.9 and 3.5 mS cm^{-1}, respectively, compared to 2.0 mS cm^{-1} for BC. The results indicate that the ion conduction is intensively facilitated by the MOFs because they store more liquid electrolytes and effectively help the ion dissociation, as revealed before. The slightly higher ionic conductivity for UiO-66@BC is because of the greater surface area of UiO-66 than that of NH_2-UiO-66 for accommodating more liquid electrolytes inside.

Li^+ transference number is a critical metric to the ion-deposition stability and is measured by using the chronoamperometry method. The current–time curves and the Nyquist plots before and after the polarization for NH_2-UiO-66@BC are shown in Figure 2e. The interfacial resistance before and after the polarization (R_o and R_{ss}), and the initial and steady-state currents (I_o and I_{ss}) are used to calculate the Li^+ transference number (see Table S2, Supporting Information, for the detailed values). As summarized in Figure 2f, the Li^+ transference number of NH_2-UiO-66@BC, UiO-66@BC, BC, and CS shows a downward trend of 0.82, 0.77, 0.60, and 0.37, respectively. The polar groups of BC can trap electrolyte solvent molecules (EC and EMC) to restrict the migration of anions, thus, to increase the Li^+ transference number.[67,68] Importantly, comparing the two MOF@BCs, we find that NH_2-UiO-66@BC delivers a higher Li^+ transference number than UiO-66@BC. This is because the anionphilic $-NH_2$ group from the linker of NH_2-UiO-66 strengthens the immobilization of anions by forming hydrogen bonding with PF_6^-.[8] In a word, both MOF@BC composite GEs exhibit higher performances in ionic conductivity and Li^+ transference number compared to CS and unmodified BC. With varying contents of NH_2-UiO-66, the ionic conductivity and Li^+ transference number are affected. As shown in Figure S9, Supporting Information, the ionic conductivities of the GEs with 10, 20, and 30 wt% NH_2-UiO-66 are 0.77, 1.0, and 0.84 mS cm^{-1}, respectively. The decrease of ionic conductivity for the 30 wt% MOF content is due to the agglomeration of MOF particles, which impedes the ion-conduction pathways. It is also found that the Li^+ transference number is increased with the MOF content; the values of the GEs with 10, 20, and 30 wt% NH_2-UiO-66 are 0.75, 0.82, and 0.88, respectively.

To help with the mechanistic understanding, the schemes are illustrated in Figure 2g. CS made of polypropylene and polyethylene is plagued by poor electrolyte wetting because of its nonpolar surface property. The ion-conduction pathways of CS are scarce, resulting in low ionic conductivity. CS also has a low Li^+ transference number due to the solvation effect of Li^+ in aprotic electrolyte solvents, which limits the motion of Li^+ in the electrolyte. For BC, the highly porous structure and rich polar groups (e.g., −OH) improve the electrolyte wetting and uptake, generating more ion-conduction pathways and higher ionic conductivity. Meanwhile, the polar groups capture the electrolyte solvents to restrict the anion migration, which increases the Li^+ transference number. As a further improvement, NH_2-UiO-66 not only facilitates the ion conduction but also helps trap anions. Specifically, the Lewis acid sites of NH_2-UiO-66 generate interactions with $PF6^-$ anions to promote the dissociation of Li salts and anchoring of anions; the anionphilic $-NH_2$ group provides further immobilization effect for the anions. This effect is further probed by measuring the Li^+ transference number of the liquid electrolyte with MOF particles dispersed (the content of MOF particles was fixed as 5 wt%). The Li^+ transference number of pristine electrolyte, UiO-66/electrolyte and NH_2-UiO-66/electrolyte is 0.54, 0.66, and 0.73, respectively, as shown in Figure S10, Supporting Information. The results are supportive to the data of the Li^+ transference number of GEs that NH_2-UiO-66@BC shows the greatest Li^+ transference number of 0.82. As a result, high ionic conductivity and high Li^+ transference number are simultaneously achieved.

The electrochemical stability window is vital for screening the suitable cathodes to be paired with GEs. The linear sweep voltammetry (LSV) results are shown in **Figure 3**a. It can be seen that the oxidation process initiates at 4.1 and 4.2 V for BC and CS, respectively. The electrochemical stability significantly increases for the two MOF@BC GEs without abrupt current increase before 5.0 V. The more focused regions are shown in Figure 3b, which shows that the two MOF@BC GEs afford electrochemical stability until 4.9 V. It is noted that the electrochemical stability of BC is poorer than that of CS, indicating the oxidation of BC prior to the liquid electrolyte. To gain a deeper insight into the reactions, the highest occupied molecular orbital (HOMO) and the lowest occupied molecular orbital (LUMO) energy levels of electrolyte components (electrolyte solvents (EC and EMC) and $LiPF_6$) and cellulose constructed with three units are calculated in Figure 3c. As shown, the cellulose demonstrates much higher HOMO than that of EC, EMC, and $LiPF_6$, implying that cellulose participates in the interface reaction prior to the electrolyte. The reaction possibly occurs from the ether oxygens. The addition of MOFs enhances the electrochemical stability owing to the high stability of MOFs to improve the interface. More importantly, the entanglement between MOFs and cellulose nanofibrils forms hydrogen bonding between $-NH_2$/−COOH groups of MOFs and ether oxygens of BC, which protects the ether oxygens from oxidation. The exceptional electrochemical stability of the composite MOF@BC GEs will benefit their applications under high voltage.

Considering that NH_2-UiO-66@BC shows comparable comprehensive properties with UiO-66@BC but a higher Li^+ transference number, we focused on NH_2-UiO-66@BC for further analysis. The differential scanning calorimetry (DSC) curves in Figure 3d show that there are two endothermic peaks at 135 °and 163 °C for the thermal decomposition of CS, attributed to the melting of polyethylene and polypropylene, respectively. However, NH_2-UiO-66@BC exhibits no significant endothermic or exothermic behaviors up to 180 °C, demonstrating its good thermal stability. The photos in Figure 3e show that CS experiences a severe shrinkage after being treated at 160 °C for 20 min, while NH_2-UiO-66@BC retains its original shape after the same treatment. After 1-h thermal treatment, NH_2-UiO-66@BC still retains good structural integrity and mechanical flexibility, further confirming the excellent thermal stability. Mechanical properties are important for GEs to generate stable interfaces with electrodes, which are measured by tensile test (Figure S11, Supporting Information). As shown in Figure 3f, the tensile strength and Young's modulus of NH_2-UiO-66@BC are 5.9 and 132.9 MPa, respectively, which are significantly

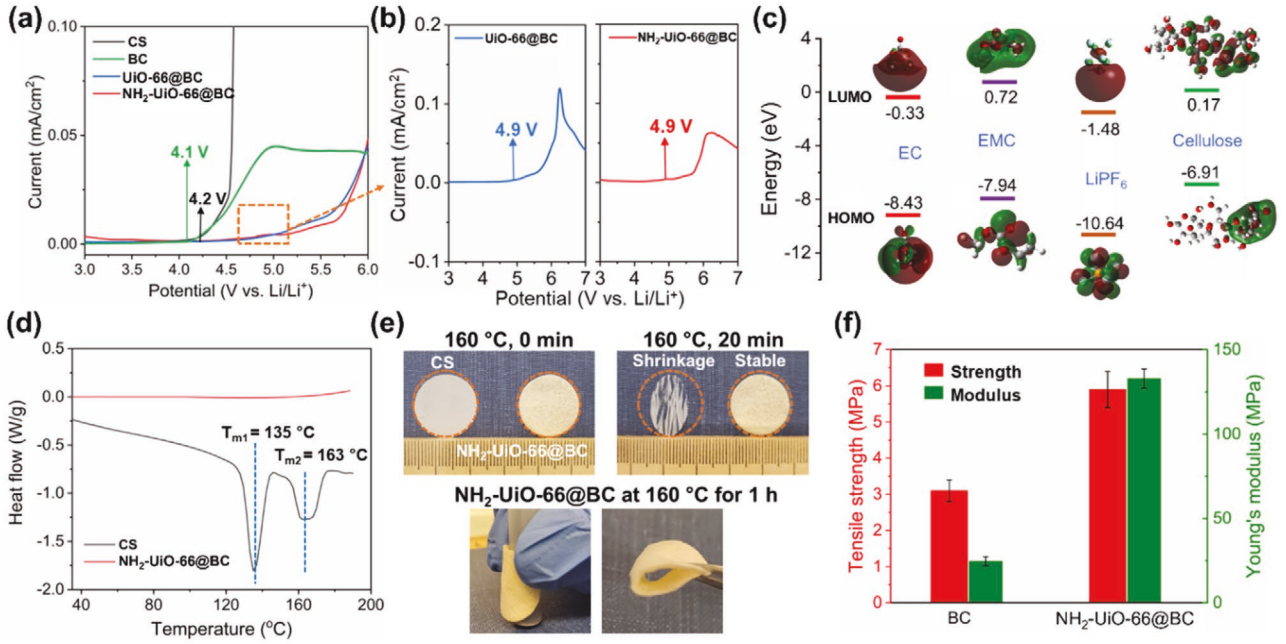

Figure 3. Electrochemical stability and thermal/mechanical properties. a) Electrochemical stability window obtained from linear sweep voltammetry (LSV) at 2 mV s^{-1}. b) Magnified region of UiO-66@BC and NH_2-UiO-66@BC. c) HOMO and LUMO energy levels of electrolyte solvents, $LiPF_6$, and cellulose (represented by three units). d) DSC curves of NH_2-UiO-66@BC compared with CS. e) Digital photos showing the thermal stability of NH_2-UiO-66@BC compared with CS. f) Tensile strength and Young's modulus of NH_2-UiO-66@BC compared with BC.

greater than that of BC (3.1 and 24.6 MPa). This is owing to the reinforcement from the NH_2-UiO-66 nanoparticles that have much higher mechanical strength than BC.

The Li plating/striping behaviors are studied to understand the contribution of the GEs to stabilizing Li anodes. As shown in **Figure 4**a, the overpotential of the symmetrical cell with NH_2-UiO-66@BC commences at ≈56 mV and then continues to decrease and remains stable around 40 mV. However, the cell with CS shows severely fluctuated overpotential after ≈200 h, which suddenly increases to 202 mV; the overpotential keeps increasing afterward. This is due to the repeated breakage/repair of the SEI layer, accumulation of "dead" Li species, and the gradual consumption of the electrolyte/Li source, greatly increasing the cell resistance.[69] A local or micro-short circuiting occurs after ≈430 h as indicated by the significant decrease of overpotential mainly because Li dendrites puncture the separator. BC delivers more stable overpotential than the case of CS, yet the value of it is obviously greater than that of NH_2-UiO-66@BC. This is because NH_2-UiO-66@BC has a higher ionic conductivity and is more effective in regulating ion deposition to diminish the dendrite growth, thus, stabilizing the SEI layer. The ability of NH_2-UiO-66@BC to stabilize Li metal becomes more notable at higher current rates. At 1 mA cm^{-2}, the cell with NH_2-UiO-66@BC still delivers a stable overpotential of ≈74 mV, while the overpotential of BC is ≈139 mV and is unstable in comparison. The magnified voltage profiles are shown in Figure 4b, indicating that both BC and NH_2-UiO-66@BC deliver flat overpotentials due to the smooth ion deposition and fast ion transfer, while noticeable bumps and dips are found for CS. The overpotential of NH_2-UiO-66@BC is always lower than that of BC. The results imply that the symmetrical cell with NH_2-UiO-66@BC obtains more stable and thinner SEI layers to avoid the depletion of the electrolyte and Li source.

The interface evolution of the symmetrical Li cells is investigated by electrochemical impedance spectroscopy (EIS) at various cycles. The equivalent circuit and fitting data are presented in Figure S12 and Table S3, Supporting Information. The interception with the horizontal axis represents the bulk resistance (R_b); the semicircle at high frequencies is attributed to the resistance of the passivation film on the Li anode (R_{SEI}), while the semicircle at low frequencies is attributed to the charge-transfer interfacial resistance (R_{CT}).[70] The fitting results in Table S3, Supporting Information, show that all cells after cycling experience decreased resistances compared to their fresh states because the interface becomes stabilized during cycling. Specifically, at the 20th cycle, the R_{CT} for CS, BC, and NH_2-UiO-66@BC shows a decreasing trend of 11.3, 16.0, and 17.0 Ω, respectively, and changes to 21.9, 15.6, and 11.1 Ω at the 40th cycle. The much lower charger–transfer resistance for BC and NH_2-UiO-66@BC is due to the improved ionic conductivity to facilitate the charge–transfer process. The R_{SEI} of the symmetrical cells shows a more obvious variation over cycling, indicating the drastic evolution of SEI layers. In the 20th cycle, the R_{SEI} of the cell with NH_2-UiO-66@BC is as low as 12.9 Ω, in comparison to 42.0 and 58.8 Ω for BC and CS, respectively. At the 40th cycle, the R_{SEI} of the CS cell sharply decreases to 16.9 Ω, possibly because of the local short-circuiting; the R_{SEI} of NH_2-UiO-66@BC is 16.5 Ω, which is still much lower than that of BC (44.2 Ω). The results show that the cell with NH_2-UiO-66@BC shows relatively stable and much lower R_{SEI} than the other two cells. It is concluded that the SEI layer is effectively stabilized by NH_2-UiO-66@BC with a high Li^+ transference number that imparts the capability for homogenizing the ion deposition to prevent the dendrite growth.

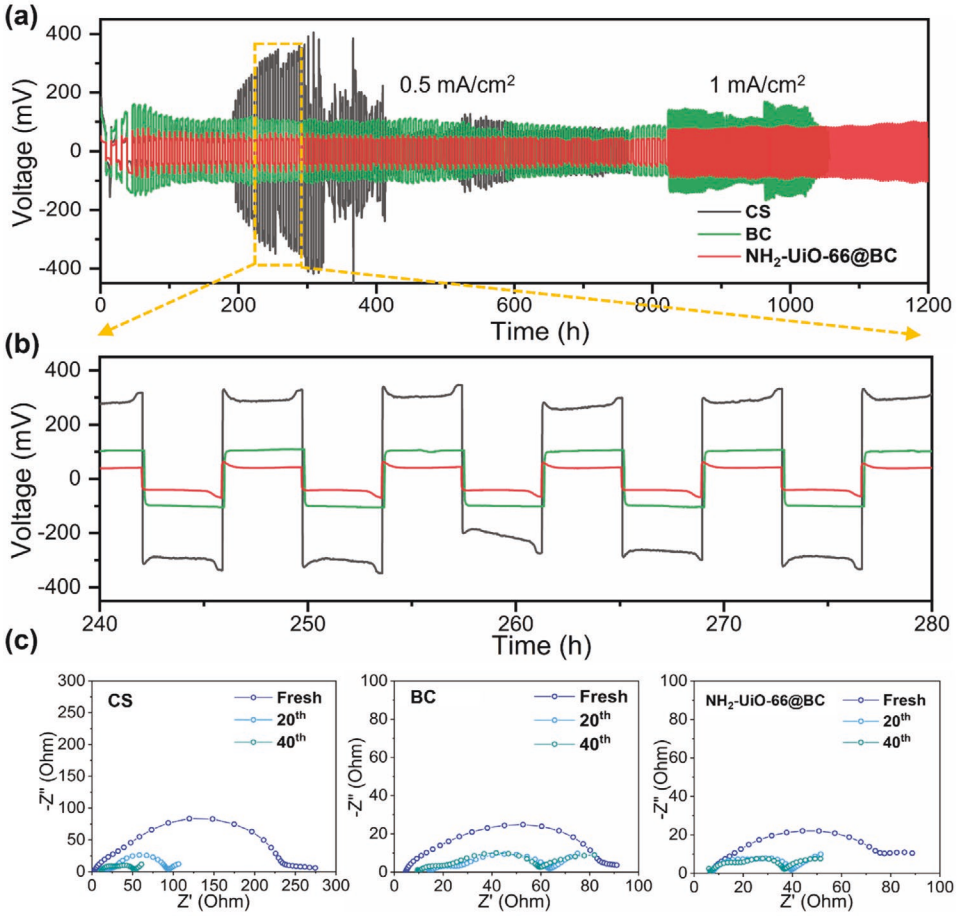

Figure 4. Li plating/striping behaviors studied in symmetrical Li cells. a) Voltage profiles at various current densities. The deposition capacity was 2 mAh cm^{-2}. b) Magnified region of selected voltage profiles. c) Nyquist plots of the cells tested at certain cycles.

The post-mortem analysis is performed to investigate the morphology of cycled Li anodes. As shown in **Figure 5**a, after 300 cycles, numerous needle-like Li dendrites and "dead" Li particles appear on the surface of Li anodes with CS and BC. On the contrary, the surface is much smoother in the case of NH_2-UiO-66@BC, and the Li metal is covered by relatively uniform SEI layers. These results are in agreement with the Li plating/striping behaviors in Figure 4. As illustrated in Figure 5b, the diffusion of Li^+ and counter anions across CS is nonuniform, resulting in inhomogeneous ion deposition and an uneven electric field to initiate the formation and propagation of dendrites. In the case of BC, even though the ion-conduction process is facilitated and the ion-deposition stability is improved, owing to the increased ionic conductivity/Li^+ transference number, the effectiveness in suppressing the dendrites is limited in comparison to that of NH_2-UiO-66@BC, whose ionic conductivity and Li^+ transference number are much greater than BC. As a result, BC is not able to fully prevent the dendrite growth, while NH_2-UiO-66@BC can well stabilize Li metal in the long term, as indicated by the more stable cycling performance as discussed in Figure 4.

The GEs are paired with $LiFePO_4$ cathodes to investigate their electrochemical performance in half cells. The voltage profiles from the initial cycle in **Figure 6**a show that all cells have steady discharge voltage plateaus at ≈3.4 V due to the redox reaction of Fe^{2+}/Fe^{3+}. The cell with NH_2-UiO-66@BC delivers the greatest discharge capacity of 169 mAh g^{-1} compared to UiO-66@BC (165 mAh g^{-1}), BC (153 mAh g^{-1}), and CS (145 mAh g^{-1}). It is also noted that except for the cell with NH_2-UiO-66@BC, the other three cells exhibit obvious dips in the discharge plateaus as referred by the arrow, which indicates that they undergo significant polarization during the discharge process in contrast to the NH_2-UiO-66@BC cell. The voltage curves of the NH_2-UiO-66@BC cell at various current rates are presented in Figure 6b. As shown at 0.2 and 0.3 C, the voltage plateaus remain smooth and flat; slight dips appear when the current rates increase to 0.5 or 1 C, indicating that the polarization is reduced by NH_2-UiO-66@BC.

The Nyquist plots of the half cells are shown in Figure 6c. The semicircle at the medium frequencies is attributed to the charge–transfer resistance (R_{CT}) and the straight line at low frequencies is attributed to the Warburg impedance (Z_W) from the Li^+ diffusion in the bulk (see the equivalent circuit in Figure S13, Supporting Information).[71] As shown, the R_{CT} of the cells with CS, BC, UiO-66@BC, and NH_2-UiO-66@BC obey a downward trend of 128, 104, 95, and 92 Ω, respectively. The tendency is basically consistent with the ionic conductivity and Li^+ transference number results. The rate capability in Figure 6d also underlines the advantage of NH_2-UiO-66@BC to

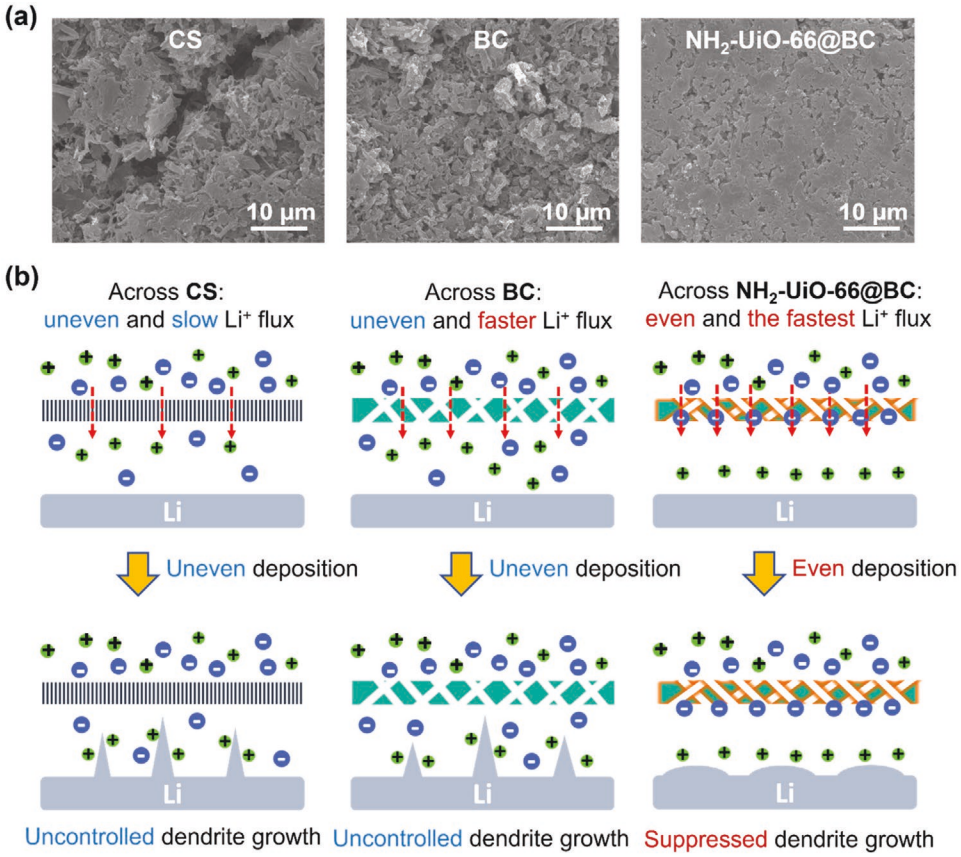

Figure 5. Regulating the ion-deposition by NH_2-UiO-66@BC to suppress dendrite growth. a) SEM images of Li metals disassembled from the cells with CS, BC, or NH_2-UiO-66@BC operated for 300 cycles at 0.5 mA cm^{-2}. b) Schematic illustration of the distribution of ion-flux and ion-deposition process for the batteries with CS, BC, or NH_2-UiO-66@BC.

enhance the battery performance, showing that the cell with NH_2-UiO-66@BC delivers the greatest discharge capacities among all cells. Specifically, at various current rates from 0.1 to 1 C, the discharge capacities are ≈169, 163, 157, 152, and 138 mAh g^{-1}, which are greatly higher than the others. The good abilities of NH_2-UiO-66@BC to conduct ions and regulate the ion deposition promote the ion-transfer process and minimize the concentration gradient/polarization, bringing about excellent performance at high current rates. Namely, at 1 C, the capacities of the cells with NH_2-UiO-66@BC, UiO-66@BC, BC, and CS are 138, 133, 120, and 108 mAh g^{-1}, respectively.

The long-term cycle stability of all cells is compared in Figure 6e. We observe that the capacity of all cells fluctuates noticeably during cycling, which is possibly attributed to the temperature change in the environment that impacts the charge/discharge process. It can be seen that the cells generally yield stable cycling performance, and no significant capacity decay is observed. At both 0.5 and 1 C, the capacities of the cell with NH_2-UiO-66@BC are the highest. At 1 C, the cell with NH_2-UiO-66@BC presents a capacity of 134 mAh g^{-1} after 200 cycles, in comparison to UiO-66@BC (118 mAh g^{-1}), BC (102 mAh g^{-1}), and CS (97 mAh g^{-1}). The excellent battery performances are contributed by the good comprehensive properties of NH_2-UiO-66@BC, such as the high ionic conductivity, high Li^+ transference number, and wide electrochemical stability window.

Next, the electrochemical performance of the GEs is investigated in the NCA system under a high cut-off voltage of 3.0–4.8 V. As shown in **Figure 7**a, at the initial cycle with 0.1 C, the three cells show similar charge/discharge curves, but the discharge capacities vary, which are 187, 177, and 170 mAh g^{-1} for NH_2-UiO-66@BC, BC, and CS, respectively. The initial Coulombic efficiencies for the cells with NH_2-UiO-66@BC, BC, and CS are 89, 83, and 86%, respectively. The low initial Coulombic efficiency of the cell with BC is due to the oxidation of BC under the high voltage; the decomposition occurs most likely from the ether oxygens, which generates irreversible capacity. At varying current rates even up to 2 C, the voltage curves of the cell with NH_2-UiO-66@BC remain stable and smooth, indicating the reversible electrochemical reactions under various current rates in spite of the capacity fading in Figure S14, Supporting Information.

Additionally, the advantage of NH_2-UiO-66@BC becomes predominant at higher current rates. As shown in Figure 7b, the NH_2-UiO-66@BC cell exhibits exceptional capacities compared to the cells with BC and CS. The capacities of the NH_2-UiO-66@BC cell at 0.1, 0.2, 0.3, 0.5, 1, and 2 C are ≈185, 170, 164, 154, 139, and 123 mAh g^{-1}, respectively. The corresponding values of the CS cell are 173, 152, 135, 113, 89, and 37 mAh g^{-1}, respectively, all of which are inferior to the NH_2-UiO-66@BC cell. It is worth noting that the capacities of the cells with CS

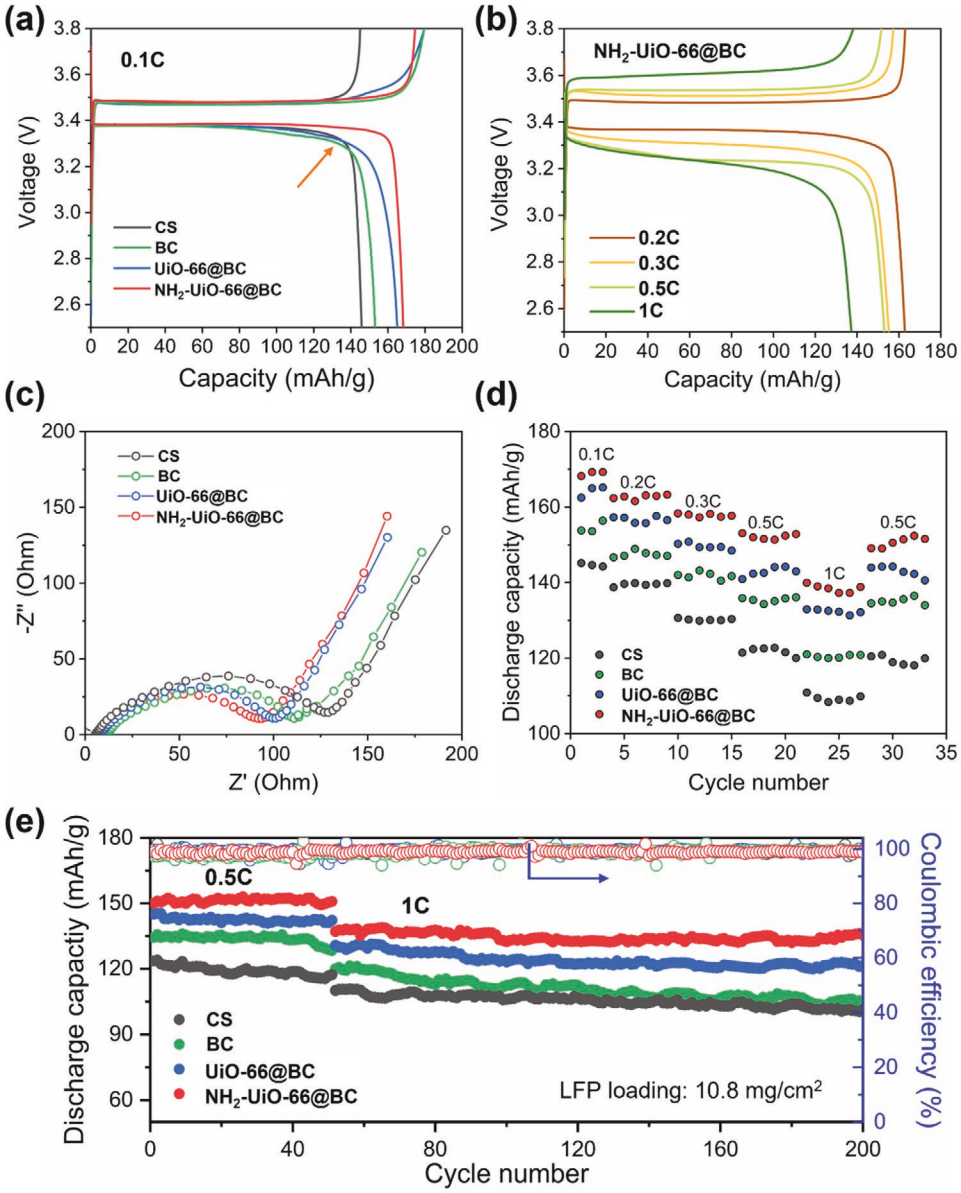

Figure 6. Electrochemical performance of $LiFePO_4$|Li cells. a) Voltage profiles of various GEs compared with CS at 0.1 C. b) Voltage profiles of NH_2-UiO-66@BC at various current rates. c) Nyquist plots of various fresh $LiFePO_4$|Li cells. d) Rate performance and e) cycle stability of various GEs compared with CS.

and BC undergo a drastic decay from 1 to 2 C, but in contrast, the cell with NH_2-UiO-66@BC only shows a slight reduction. After recovering the current rate from 2 to 0.5 C, the capacity retentions are 96%, 93%, and 83%, respectively, for the cells with NH_2-UiO-66@BC, BC, and CS. The cycle performance in Figure 7c shows that the CS cell suffers from a notable capacity fading after about 50 cycles, while the cells with NH_2-UiO-66@BC and BC deliver much stable and higher capacities; specifically, the cell with NH_2-UiO-66@BC shows the highest capacities throughout the cycling. After 100 cycles at 1 C, the capacities for the cells with CS, BC, and NH_2-UiO-66@BC are 124, 105, and 71 mAh g^{-1}, respectively, corresponding to the capacity retentions of 62%, 84%, and 83%. It is also seen that the three cells show fluctuation of the Coulombic efficiency under high voltage, but the fluctuation degree of NH_2-UiO-66@BC is much less intensive than the other two. Considering that the electrochemical stability of CS and BC is much lower than 4.8 V (the cut-off charge voltage), we attribute the fluctuation to the electrolyte oxidation. The above results further prove the superiority of the NH_2-UiO-66@BC GE to stabilize the electrode/electrolyte interface even under high voltage, in addition to accelerating the ion-conduction kinetics.

The cathode/electrolyte interphase (CEI) composition of the cycled NCA is examined by X-ray photoelectron spectroscopy (XPS) in Figure 7d,e. The high-resolution C 1s spectra in Figure 7a show five deconvolution peaks. The peaks at 286.1 eV (C—O), 287.4 eV (C=O), and 289.9 eV ($ROCO_2Li$) originate from the decomposition products of carbonate electrolyte solvents

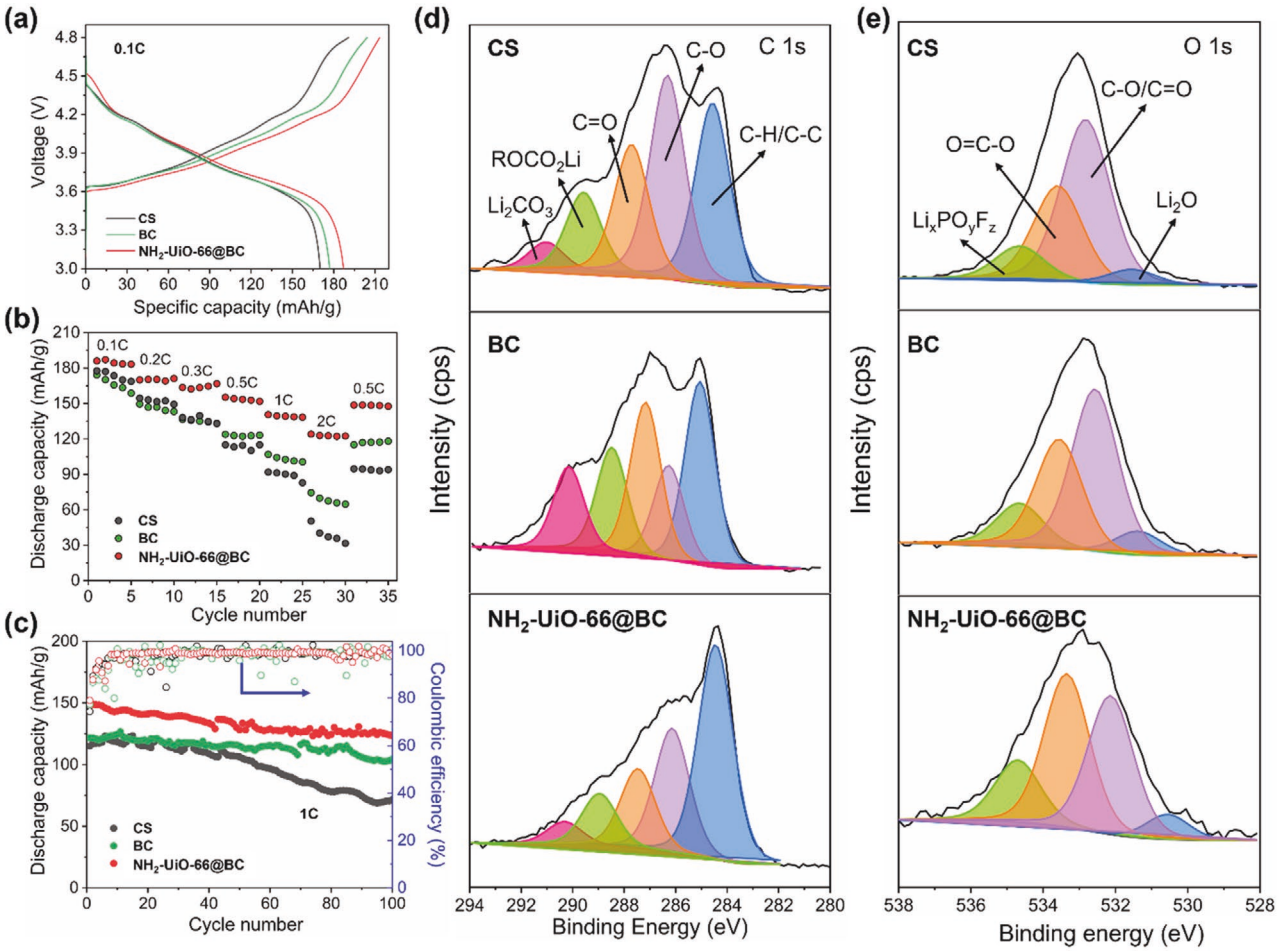

Figure 7. Electrochemical performance of NCA|Li cells. a) Voltage profiles of various GEs compared with CS at 0.1 C. The cut-off voltage was 3–4.8 V. b) Rate performance and c) cycle stability of various GEs compared with CS. The cycle stability was measured at 1 C. High-resolution d) C 1s and e) O 1s XPS spectra of NCA electrodes operated for 100 cycles at 1 C.

(EC/EMC) by ring-opening and polymerization.[72] The decomposition of BC may also generate $ROCO_2Li$.[59] The detailed compositions are shown in Figure S15, Supporting Information, which indicates that the total composition of C—O, C=O, and $ROCO_2Li$ in the CEI for NH_2-UiO-66@BC is 55.8%, which is fewer than that of BC (59.2%) and CS (61.6%). The results manifest that the decompositions of electrolyte/BC are effectively suppressed by the NH_2-UiO-66@BC GE due to the better accommodation of the liquid electrolyte and the reduced amount of free electrolyte molecules as well as the protection of the ether oxygens. In Figure 7e, there are four deconvolution peaks at 531.9 eV (Li_2O), 532.8 eV (C—O/C=O), 533.4 eV (O=C—O), and 534.5 eV ($Li_xPO_yF_z$) in the O 1s spectra. The detailed compositions show that the CEI from the NCA cathode with NH_2-UiO-66@BC has less amount of C—O/C=O/O—C=O (49.5%) compared to BC (52.8%) and CS (54.0%). The finding is consistent with the data of the C1s spectra, confirming the least decompositions of the electrolyte and BC from the NH_2-UiO-66@BC GE. The SEM images of NCA cathodes operated for 100 cycles are displayed in Figure S16, Supporting Information. The results show that numerous film-like decomposition products form on the surface of the cathodes with CS and BC, but the cathode with NH_2-UiO-66@BC basically retains its original morphology and is covered by less amount of decomposition products. These advantages significantly contribute to the performance enhancement for high-voltage cathodes.

3. Conclusion

In summary, we report MOF@BC composite aerogels as the GE matrices to regulate ion deposition and facilitate ion conduction so as to effectively suppress Li dendrites and stabilize LMBs under high voltage. Two hierarchically mesoporous Zr-based MOFs with different organic linkers, that is, UiO-66 and NH_2-UiO-66, are composited with BC nanofibrils to fabricate the 3D porous composite aerogels. It is found that the anionphilic linkers of NH_2-UiO-66 act as extra anion-immobilization sites, making it more effective in regulating ion deposition; NH_2-UiO-66 also protects BC from oxidation under high voltage by forming intermolecular interactions to broaden the electrochemical stability window. The resulting NH_2-UiO-66@BC GE exhibits high ionic conductivity (≈1 mS cm^{-1}), high Li^+ transference number (0.82), good electrochemical stability up to 4.9 V,

and good thermal stability. As a result, the symmetrical Li cell delivers a long cycling life of ≈1200 h. The NH_2-UiO-66@BC GE significantly improves the electrochemical performances of the batteries with $LiFePO_4$ or NCA cathodes. Specifically, under a high operation voltage, the cathode/electrolyte interphase is effectively stabilized by the NH_2-UiO-66@BC GE that diminishes the electrolyte decomposition. This study imparts a rational design of multifunctional, high voltage-compatible, and environmentally-friendly GEs for addressing the critical challenges of LMBs under broad operation conditions.

4. Experimental Section

Preparation of Bacterial Cellulose Dispersion: Industrial grade bacterial cellulose (BC) was provided by Hainan Laize Biochemical Co., China. The BC sheets were crunched into small pieces and purified by copious 1 M KOH solution at 80 °C for 10 h. The BC pieces were then rinsed with deionized water several times and physically crushed in deionized water at 10 000 rpm per min to form a suspension. Acetone with the same volume of water was added into the suspension, which stood at room temperature for 24 h. The solvents were removed by suction filtration, and the remnant was rinsed with ethanol and deionized water successively. The obtained BC samples were then dispersed in deionized water with a solid content of 0.5 wt%.

Preparation of Metal–Organic Framework Materials: The compound UiO-66 was synthesized through the modification of previously reported literature.[73] Terephthalic acid (BDC) (0.3777 g, 2.3 mmol) and $ZrOCl_2{\cdot}8H_2O$ (0.731 g, 2.3 mmol) were dissolved in 250 mL of *N,N*-dimethylformamide (DMF) giving a clear solution. Next, 25 mL aliquots of solution were added into 30 mL scintillation vials before being capped and placed in an oven at 135 °C for 48 h. The resulting product was an opaque clear gel. The gel precipitate was separated from the solution using a centrifuge and washed three times with 30 mL of DMF, and then the sample was allowed to soak for 24 h in fresh DMF. Next, the product was washed three times with 30 mL of MeOH and then soaked for four days in MeOH. During this period, the MeOH was exchanged once every day. The washed product was removed from the solution using a centrifuge and dried in a gravity oven at 85 °C for 48 h. The dried product was a singular white solid and was ground using a mortar and pestle to obtain a fine white powder.

The compound NH_2-UiO-66 was synthesized in a similar manner as above but with the following changes. 2-aminoterepthahlic acid (0.412 g, 2.3 mmol) and $ZrOCl_2{\cdot}8H_2O$ (0.732 g, 2.3 mmol) were dissolved in 250 mL of DMF, giving a transparent yellow solution. Next, 25 mL aliquots of the prepared solution were added to 30 mL scintillation vials. The vials were sealed and subsequently placed in a preheated 120 °C oven for 24 h. The resultant product was an opaque gel. After cooling the vial to room temperature, the synthesized precipitate was obtained by centrifugation and was washed three times with 30 mL of DMF. The product was then soaked in fresh DMF for 24 h. After this, the precipitate was washed three times with 30 mL of MeOH and soaked for four days in MeOH. The MeOH was exchanged every 24 h. The solid product was separated from the solution using a centrifuge and was dried in a gravity oven at 85 °C for 48 h. The dried product was a single yellow solid and was ground using a mortar and pestle to obtain a fine yellow powder.

Preparation of BC Aerogel and MOF@BC Composite Aerogels: The MOF nanoparticles were pre-dispersed in deionized water by tip ultrasonication with an amplitude of 15% for 30 min in an ice bath. Then, the MOF suspension was added to the BC suspension, and the resulting mixture was treated by bath ultrasonication for 2 h. The solid content of MOF nanoparticles was kept constant to be 20 wt%. The mixture suspension was poured into glass petri dishes, frozen in liquid nitrogen for 12 h, and freeze-dried at −50 °C for 24 h. Then, the prepared composite aerogels were compressed using a hot-press machine with a pressure of 10 MPa to obtain the gel electrolyte matrix at room temperature. To prepare the BC aerogel, the procedures were the same as above except that the MOF nanoparticles were not added into the BC dispersion.

Materials Characterizations: *Morphologies, Structures, and Mechanical/Thermal Stabilities*: Morphologies were investigated by using scanning electron microscopy (SEM, Quanta 200F) and transmission electron microscopy (TEM, FEI T20). Pore structures and surface area of MOFs were measured by N_2 adsorption–desorption analysis using Micromeritics ASAP 2020 Plus at 77 K. Crystalline structures were investigated by X-ray diffraction (XRD) (Rigaku Miniflex 600) using Cu Kα radiation from 5° to 40°. Surface functional groups were investigated by Fourier-transform infrared (FTIR) spectroscopy (Nicolet iS10, Thermo Fisher) with attenuated total reflectance (ATR) mode. The tensile test was performed by dynamic mechanical analysis (DMA, Q800, TA Instruments) using a film mode with a strain of 2% at room temperature. The thermal properties were studied by differential scanning calorimetry (DSC, Mettler Toledo) under an N_2 atmosphere with a heating rate of 10 °C min^{-1}; the temperature range was 25 °C to 180 °C. Thermogravimetric analysis (TGA, Mettler Toledo) was conducted under N_2 flow with a heating rate of 10 °C min^{-1} from 25 °C to 600 °C. The thermal shrinkage behavior was monitored by placing the separator or aerogel samples on the hot plate with a surface temperature of 160 °C. The contact angle was measured by optical contact angle analyzer (OCA 15 plus, Dataphysics Instruments). Each sample was measured three times for consistency. To probe the compositions of the cathode/electrolyte interphase, the NCA cathodes were harvested from cycled batteries and then rinsed by the ethyl methyl carbonate (EMC) solvent several times to remove the residual Li salt. The cathodes were dried in the vacuum chamber of the glove box for 12 h and then quickly transferred for measurement. The surface elements of NCA cathodes were investigated by X-ray photoelectron spectroscopy (XPS, K-Alpha, Thermo Fisher) using monochromated Al Kα radiation.

Electrochemical Characterizations: *Electrochemical Properties*: The liquid electrolyte consisted of 1 M $LiPF_6$ in a mixture solvent of ethylene carbonate (EC) and ethyl methyl carbonate (EMC) (1:1 by volume). The electrolyte uptake (U) was determined by Equation (1):

$$U = \frac{M_2 - M_1}{M_1} \times 100\% \tag{1}$$

where M_1 and M_2 are the mass of the sample before and after adsorbing the electrolyte, respectively.

The cation–anion interaction was probed by FTIR–ATR on the liquid electrolytes with or without 20 wt% MOFs. The gel electrolytes were sandwiched by two stainless steel disks to measure their ionic conductivity. The ionic conductivity was measured by electrochemical impedance spectroscopy (EIS) using an electrochemical workstation (BioLogic VSP) over a frequency range of 0.1–10^6 Hz. The ionic conductivity was calculated from Equation (2):

$$\sigma = L / (AR_b) \tag{2}$$

where L is the thickness of the separator; A is the contact area; R_b is the bulk resistance obtained from the intersection of the horizontal axis.

The Li^+ transference number (t^+) was measured by using the chronoamperometry method based on Li/Li cells with a polarization voltage of 50 mV. The Li^+ transference number was calculated from Equation (3):

$$t^+ = \frac{I_{SS}(\Delta V - I_0 R_0)}{I_0(\Delta V - I_{ss} R_{ss})} \tag{3}$$

where I_0 and I_{ss} are the initial and steady-state currents, respectively; R_0 and R_{ss} are the interfacial resistance before and after the AC polarization, respectively.

Battery Performance: Electrode slurries were composed of 80 wt% $LiFePO_4$ (LFP) or $LiNiCoAlO_2$ (Ni:Co:Al = 8.15:1.5:0.35, NCA), 10 wt%

carbon black (SuperC45), and 10 wt% polyvinylidene fluoride in n-methyl-2-pyrrolidone. All the aforementioned materials were purchased from MTI Corp. The slurry was cast on a carbon-coated aluminum foil and dried at 90 °C in a vacuum oven for 12 h. The loading of active materials was 10.8 and 10 mg cm^{-2} for LFP and NCA, respectively. Coin cells (CR-2032) were assembled using the Li metal chip with a thickness of 60 µm as the anode. The resulting cells were cycled with a cut-off voltage of 2.5–3.8 V (LFP) or 3.0–4.8 V (NCA) using a battery analyzer (BST8-MA, MTI Corp.).

Symmetrical Li cells were assembled by using Li metal chips as both the working and reference electrodes. The electrolyte volume was kept constant at 60 µL. The cells were cycled between –0.1 and 0.1 V with a fixed deposition capacity of 2 mAh cm^{-2}. The current densities were 0.5 or 1 mA cm^{-2} for long-term cycling. In the initial five cycles, the cells were activated and stabilized at a small current density of 0.5 mAh cm^{-2}. The EIS spectra of the cells under discharge state were recorded at certain cycle numbers using an electrochemical workstation over a frequency range of 0.01–10^6 Hz.

Supporting Information

Supporting Information is available from the Wiley Online Library or from the author.

Acknowledgements

The authors would like to acknowledge the financial support by NSF CBET 1929236 and the support in microscopy characterizations from the Franceschi Microscopy & Imaging Center at the Washington State University. Q.Z. is thankful for the financial support from the ACS Petroleum Research Fund, Award number: 60705-DNI10. In addition, M.J.H. is thankful for the financial support from the Donald S. Matteson Graduate Fellowship at the Washington State University.

Conflict of Interest

The authors declare no conflict of interest.

Data Availability Statement

The data that support the findings of this study are available on request from the corresponding author. The data are not publicly available due to privacy or ethical restrictions.

Keywords

aerogels, bacterial cellulose, gel electrolyte, lithium metal batteries, metal–organic frameworks

Received: October 13, 2021
Revised: November 15, 2021
Published online: December 15, 2021

[1] H. Hong, N. A. R. Che Mohamad, K. Chae, F. Marques Mota, D. H. Kim, *J. Mater. Chem. A* **2021**, *9*, 10012.
[2] X. Fu, W.-H. Zhong, *Adv. Energy Mater.* **2019**, *9*, 1901774.
[3] L. Chen, X. Fan, X. Ji, J. Chen, S. Hou, C. Wang, *Joule* **2019**, *3*, 732.
[4] S. S. Zhang, *J. Power Sources* **2013**, *231*, 153.
[5] X. Gao, Y. Chen, L. Johnson, P. G. , Bruce, *Nat. Mater.* **2016**, *15*, 882.
[6] Y. Lee, T. K. Lee, S. Kim, J. Lee, Y. Ahn, K. Kim, H. Ma, G. Park, S.-M. Lee, S. K. Kwak, N.-S. Choi, *Nano Energy* **2020**, *67*, 104309.
[7] Y. Tang, L. Zhang, J. Chen, H. Sun, T. Yang, Q. Liu, Q. Huang, T. Zhu, J. Huang, *Energy Environ. Sci.* **2021**, *14*, 602.
[8] X. Fu, R. Odstrcil, M. Qiu, J. Liu, W.-H. Zhong, *Energy Storage Mater.* **2021**, *42*, 22.
[9] M. Rosso, C. Brissot, A. Teyssot, M. Dollé, L. Sannier, J.-M. Tarascon, R. Bouchet, S. Lascaud, *Electrochim. Acta* **2006**, *51*, 5334.
[10] H. Mao, W. Yu, Z. Cai, G. Liu, L. Liu, R. Wen, Y. Su, H. Kou, K. Xi, B. Li, H. Zhao, X. Da, H. Wu, W. Yan, S. Ding, *Angew. Chem., Int. Ed.* **2021**, *60*, 19306.
[11] H. Liu, X. Yue, X. Xing, Q. Yan, J. Huang, V. Petrova, H. Zhou, P. Liu, *Energy Storage Mater.* **2019**, *16*, 505.
[12] Q. Li, S. Zhu, Y. Lu, *Adv. Funct. Mater.* **2017**, *27*, 1606422.
[13] H. Wang, J. Wu, L. Yuan, Z. Li, Y. Huang, *ACS Appl. Mater. Interfaces* **2020**, *12*, 28337.
[14] Y. Zhong, Y. Chen, Y. Cheng, Q. Fan, H. Zhao, H. Shao, Y. Lai, Z. Shi, X. Ke, Z. Guo, *ACS Appl. Mater. Interfaces* **2019**, *11*, 37726.
[15] N.-W. Li, Y.-X. Yin, C.-P. Yang, Y.-G. Guo, *Adv. Mater.* **2016**, *28*, 1853.
[16] H. Yue, Q. Zhu, S. Dong, Y. Zhou, Y. Yang, L. Cheng, M. Qian, L. Liang, W. Wei, H. Wang, *ACS Appl. Mater. Interfaces* **2020**, *12*, 43543.
[17] X. Yin, W. Deng, X. Zhou, B. He, J. Liang, Z. Hu, F. Zhao, Z. Liu, *ACS Appl. Mater. Interfaces* **2021**, *13*, 23584.
[18] L.-y. Wei, N.-p. Deng, J.-g. Ju, H.-j. Zhao, G. Wang, H.-y. Xiang, W.-m. Kang, B.-w. Cheng, *Chem. Eng. J.* **2021**, *424*, 130346.
[19] F. Wu, Z. Wen, Z. Zhao, J. Bi, Y. Shang, Y. Liang, L. Li, N. Chen, Y. Li, R. Chen, *Energy Storage Mater.* **2021**, *38*, 447.
[20] K. Kisu, S. Kim, H. Oguchi, N. Toyama, S.-i. Orimo, *J. Power Sources* **2019**, *436*, 226821.
[21] J. Jie, Y. Liu, L. Cong, B. Zhang, W. Lu, X. Zhang, J. Liu, H. Xie, L. Sun, *J. Energy Chem.* **2020**, *49*, 80.
[22] G. Wang, X. Xiong, D. Xie, X. Fu, X. Ma, Y. Li, Y. Liu, Z. Lin, C. Yang, M. Liu, *Energy Storage Mater.* **2019**, *23*, 701.
[23] V. -C. Ho, D. T. Ngo, H. T. T. Le, R. Verma, H. -S. Kim, C.-N. Park, C.-J. Park, *Electrochim. Acta* **2018**, *279*, 213.
[24] S. Li, M. Jiang, Y. Xie, H. Xu, J. Jia, J. Li, *Adv. Mater.* **2018**, *30*, 1706375.
[25] J. Liu, H. Yuan, H. Liu, C.-Z. Zhao, Y. Lu, X.-B. Cheng, J.-Q. Huang, Q. Zhang, *Adv. Energy Mater.* **2021**, https://doi.org/10.1002/aenm.202100748.
[26] Y. Zheng, Y. Yao, J. Ou, M. Li, D. Luo, H. Dou, Z. Li, K. Amine, A. Yu, Z. Chen, *Chem. Soc. Rev.* **2020**, *49*, 8790.
[27] Q. Yang, N. Deng, J. Chen, B. Cheng, W. Kang, *Chem. Eng. J.* **2021**, *413*, 127427.
[28] W. Ren, C. Ding, X. Fu, Y. Huang, *Energy Storage Mater.* **2021**, *34*, 515.
[29] G. Chen, F. Zhang, Z. Zhou, J. Li, Y. Tang, *Adv. Energy Mater.* **2018**, *8*, 1801219.
[30] H. Fan, C. Yang, X. Wang, L. Liu, Z. Wu, J. Luo, R. Liu, *J. Electroanal. Chem.* **2020**, *871*, 114308.
[31] X. Zou, Q. Lu, Y. Zhong, K. Liao, W. Zhou, Z. Shao, *Small* **2018**, *14*, 1801798.
[32] P.-Y. Chuang, L.-Y. Chang, C.-N. Chuang, S.-H. Chen, J.-J. Lin, K.-C. Ho, K.-H. Hsieh, *J. Polym. Res.* **2016**, *23*, 214.
[33] R. Singh, S. Janakiraman, M. Khalifa, S. Anandhan, S. Ghosh, A. Venimadhav, K. Biswas, *J. Mater. Sci.: Mater. Electron.* **2020**, *31*, 22912.
[34] X. Cheng, J. Pan, Y. Zhao, M. Liao, H. Peng, *Adv. Energy Mater.* **2018**, *8*, 1702184.
[35] J. Zhou, H. Ji, J. Liu, T. Qian, C. Yan, *Energy Storage Mater.* **2019**, 256.
[36] X. Fu, Y. Wang, L. Scudiero, W. -H. Zhong, *Energy Storage Mater.* **2018**, *15*, 447.
[37] C. Monroe, J. Newman, *J. Electrochem. Soc.* **2005**, *152*, A396.

[38] C. Brissot, M. Rosso, J. N. Chazalviel, S. Lascaud, *J. Power Sources* **1999**, *81–82*, 925.
[39] Y. Wang, L. Fu, L. Shi, Z. Wang, J. Zhu, Y. Zhao, S. Yuan, *ACS Appl. Mater. Interfaces* **2019**, *11*, 5168.
[40] K. Luo, L. Yi, X. Chen, L. Yang, C. Zou, X. Tao, H. Li, T. Wu, X. Wang, *J. Electroanal. Chem.* **2021**, *895*, 115462.
[41] P. Yang, X. Gao, X. Tian, C. Shu, Y. Yi, P. Liu, T. Wang, L. Qu, B. Tian, M. Li, W. Tang, B. Yang, J. B. Goodenough, *ACS Energy Lett.* **2020**, *5*, 1681.
[42] Z. Zhang, Y. Huang, C. Li, X. Li, *ACS Appl. Mater. Interfaces* **2021**, *13*, 37262.
[43] C. -C. Sun, A. Yusuf, S. -W. Li, X. -L. Qi, Y. Ma, D. -Y. Wang, *Chem. Eng. J.* **2021**, *414*, 128702.
[44] D. -D. Han, Z. -Y. Wang, G. -L. Pan, X. -P. Gao, *ACS Appl. Mater. Interfaces* **2019**, *11*, 18427.
[45] X. Lu, H. Wu, D. Kong, X. Li, L. Shen, Y. Lu, *ACS Mater. Lett.* **2020**, *2*, 1435.
[46] D. Huang, C. Liang, L. Chen, M. Tang, Z. Zheng, Z. Wang, *J. Mater. Sci.* **2021**, *56*, 5868.
[47] A. Song, Y. Huang, X. Zhong, H. Cao, B. Liu, Y. Lin, M. Wang, X. Li, *J. Membr. Sci.* **2018**, *556*, 203.
[48] C. Ding, X. Fu, H. Li, J. Yang, J.-L. Lan, Y. Yu, W.-H. Zhong, X. Yang, *Adv. Funct. Mater.* **2019**, *29*, 1904547.
[49] P. R. Sharma, A. J. Varma, *Carbohydr. Polym.* **2014**, *114*, 339.
[50] J. Sheng, S. Tong, Z. He, R. Yang, *Cellulose* **2017**, *24*, 4103.
[51] L. Zhao, J. Fu, Z. Du, X. Jia, Y. Qu, F. Yu, J. Du, Y. Chen, *J. Membr. Sci.* **2020**, *593*, 117428.
[52] Z. Du, Y. Su, Y. Qu, L. Zhao, X. Jia, Y. Mo, F. Yu, J. Du, Y. Chen, *Electrochim. Acta* **2019**, *299*, 19.
[53] J. Wan, J. Zhang, J. Yu, J. Zhang, *ACS Appl. Mater. Interfaces* **2017**, *9*, 24591.
[54] X. Deng, Y. Huang, A. Song, B. Liu, Z. Yin, Y. Wu, Y. Lin, M. Wang, X. Li, H. Cao, *Mater. Chem. Phys.* **2019**, *229*, 232.
[55] J.-Y. Han, Y. Huang, Y. Chen, A. M. Song, X.-H. Deng, B. Liu, X. Li, M.-S. Wang, *ChemElectroChem* **2020**, *7*, 1213.
[56] F. Yu, H. Zhang, L. Zhao, Z. Sun, Y. Li, Y. Mo, Y. Chen, *Carbohydr. Polym.* **2020**, *246*, 116622.
[57] Y. S. Zhu, S. Y. Xiao, M. X. Li, Z. Chang, F. X. Wang, J. Gao, Y. P. Wu, *J. Power Sources* **2015**, *288*, 368.
[58] S. Xiao, F. Wang, Y. Yang, Z. Chang, Y. Wu, *RSC Adv.* **2014**, *4*, 76.
[59] F. J. Simon, M. Hanauer, F. H. Richter, J. Janek, *ACS Appl. Mater. Interfaces* **2020**, *12*, 11713.
[60] C. Lv, Z. Li, X. Ren, K. Li, J. Ma, X. Duan, *J. Mater. Chem. A* **2021**, *9*, 3995.
[61] S. Hu, A. S. Pillai, G. Liang, W. K. Pang, H. Wang, Q. Li, Z. Guo, *Electrochem. Energy Rev.* **2019**, *2*, 277.
[62] L. -Y. Yang, J. -H. Cao, B. -R. Cai, T. Liang, D. -Y. Wu, *Electrochim. Acta* **2021**, *382*, 138346.
[63] H. Wu, Q. Wu, F. Chu, J. Hu, Y. Cui, C. Yin, C. Li, *J. Power Sources* **2019**, *419*, 72.
[64] F. Ahmadijokani, R. Mohammadkhani, S. Ahmadipouya, A. Shokrgozar, M. Rezakazemi, H. Molavi, T. M. Aminabhavi, M. Arjmand, *Chem. Eng. J.* **2020**, *399*, 125346.
[65] Y. Luan, Y. Qi, H. Gao, N. Zheng, G. Wang, *J. Mater. Chem. A* **2014**, *2*, 20588.
[66] A. V. Cresce, S. M. Russell, O. Borodin, J. A. Allen, M. A. Schroeder, M. Dai, J. Peng, M. P. Gobet, S. G. Greenbaum, R. E. Rogers, K. Xu, *Phys. Chem. Chem. Phys.* **2017**, *19*, 574.
[67] Y. Wang, J. Qiu, J. Peng, J. Li, M. Zhai, *J. Mater. Chem. A* **2017**, *5*, 12393.
[68] A. Song, Y. Huang, X. Zhong, H. Cao, B. Liu, Y. Lin, M. Wang, X. Li, *Electrochim. Acta* **2017**, *245*, 981.
[69] J. Chang, J. Shang, Y. Sun, L. K. Ono, D. Wang, Z. Ma, Q. Huang, D. Chen, G. Liu, Y. Cui, Y. Qi, Z. Zheng, *Nat. Commun.* **2018**, *9*, 4480.
[70] S. Xia, J. Lopez, C. Liang, Z. Zhang, Z. Bao, Y. Cui, W. Liu, *Adv. Sci.* **2019**, *6*, 1802353.
[71] Y. Gao, L. Zhang, S. Feng, W. Shen, S. Guo, *J. Solid State Electrochem.* **2018**, *22*, 285.
[72] H. Lee, H.-S. Lim, X. Ren, L. Yu, M. H. Engelhard, K. S. Han, J. Lee, H.-T. Kim, J. Xiao, J. Liu, W. Xu, J.-G. Zhang, *ACS Energy Lett.* **2018**, *3*, 2921.
[73] L. Hao, X. Li, M. J. Hurlock, X. Tu, Q. Zhang, *Chem. Commun.* **2018**, *54*, 11817.